PAPER • OPEN ACCESS

Zero-frequency Bragg gap by spin-harnessed metamaterial

New Journal of Physics
The open access journal at the forefront of physics

Deutsche Physikalische Gesellschaft DPG
IOP Institute of Physics

Published in partnership with: Deutsche Physikalische Gesellschaft and the Institute of Physics

OPEN ACCESS

RECEIVED
1 May 2018

REVISED
4 July 2018

ACCEPTED FOR PUBLICATION
14 August 2018

PUBLISHED
24 August 2018

PAPER

Zero-frequency Bragg gap by spin-harnessed metamaterial

Joo Hwan Oh[1], **Seong Jae Choi**[2,3], **Jun Kyu Lee**[2] **and Yoon Young Kim**[2]

[1] School of Mechanical, Aerospace and Nuclear Engineering, Ulsan National Institute of Science and Technology, UNIST-gil 50, Eonyang-eup, Ulju-gun,Ulsan, 44919, Republic of Korea
[2] Department of Mechanical Engineering, Institute of Advanced Machines and Design, Seoul National University, 599 Gwanak-ro, Gwanak-gu, Seoul, 151-744, Republic of Korea
[3] Currently at Korea Aerospace Industries, Korea.

E-mail: yykim@snu.ac.kr

Keywords: elastic metamaterial, Bragg gap, zero-frequency, spin-harnessed metamaterial

Abstract

The Bragg gap that stops wave propagation may not be formed from zero or a very low frequency unless the periodicity of a periodic system is unrealistically large. Accordingly, the Bragg gap has been considered to be inappropriate for low frequency applications despite its broad bandwidth. Here, we report a new mechanism that allows formation of the Bragg gap starting from a nearly zero frequency. The mechanism is based on the finding that if additional spin motion is coupled with the longitudinal motion of a mass of a diatomic mechanical periodic system, the Bragg gap starting from a nearly zero frequency can be formed. The theoretical analysis shows that the effective mass and stiffness at the band gap frequencies are all positive, confirming that the formed stop band is a Bragg gap. The periodic system is realized by a spin-harnessed metamaterial which incorporates unique linkage mechanisms. The numerical and experimental validation confirmed the formation of the low-frequency Bragg gap. The zero-frequency Bragg gap is expected to open a new way to control hard-to-shield low-frequency vibration and noise.

1. Introduction

A Bragg gap is a stop band originating from destructive interferences of scattering waves in periodic structures [1, 2], such as phononic or photonic crystals. It has been applied to design various wave manipulating devices including wave-guides [3–6], frequency filters [7–10] and wave diodes [11–14]. The size of a Bragg gap can be large, but its formation at a very low frequency band has been considered theoretically impossible unless unrealistically large periodicity is considered. Due to the theoretic limit, previous research has considered other principles to form very low-frequency stop bands. In particular, resonant metamaterials have been intensively studied [15–23] because negative effective material properties attained near the resonant frequency can stop wave propagation. However, the resulting stop band is generally narrow compared with the stop band formed by the Bragg phenomenon. Other attempts using the plasmonic effects have been made to achieve ultra-low frequency stop bands. Lee *et al* [24, 25] utilized the notion of acoustic plasmonics to design acoustic metamaterials exhibiting negative material properties at quasi-static frequencies. In elasticity, Yao *et al* [26] and Yu *et al* [27] proposed elastic metamaterials supported by elastic foundations, also realizing quasi-static stop bands. However, these approaches require external fixation to the metamaterial, which is difficult to realize in general applications. Recently, Oh *et al* [28] proposed flexural elastic metamaterials based on zero rotational stiffness. However, no mechanism to form a broad Bragg gap at extremely low frequencies was explored for general periodic systems.

Through this study, we present our new mechanism to form a Bragg gap at extremely low frequencies. For the investigation, we consider longitudinal waves the polarization direction of which are parallel to their propagation directions. To explain our idea, consider a diatomic lattice consisting of two dissimilar masses (M and m, $M > m$) connected through springs of stiffness k, as shown in figure 1(a). In the diatomic lattice, the lower band-edge frequency of the Bragg gap is given by $\omega_L = \sqrt{2k/M}$ that corresponds to a standing wave

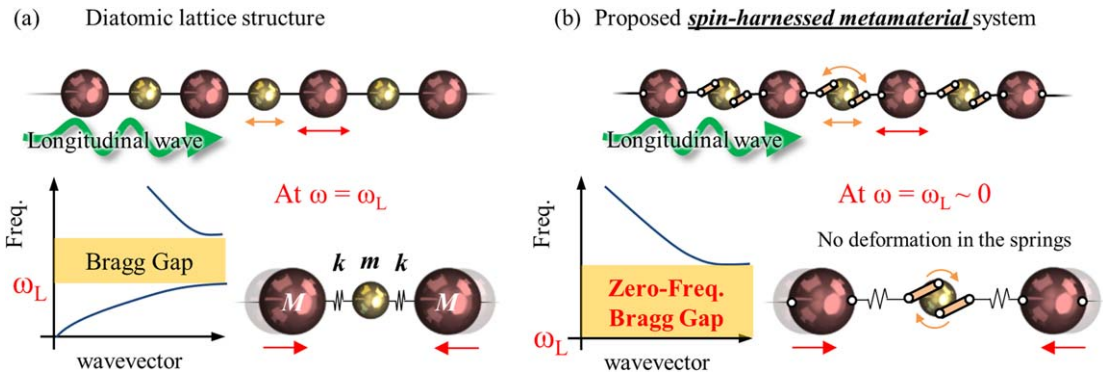

Figure 1. Comparison of (a) the conventional periodic system and (b) proposed spin-harnessed periodic system. (ω_L: the lower band-edge frequency of a Bragg gap.)

motion [29]. At ω_L, two heavier masses M in adjacent unit cells move in the opposite directions while the lighter mass m between them remains stationary. Therefore, the springs connecting M and m are compressed or stretched.

Our new mechanism is based on the idea that the lower band-edge frequency ω_L can become zero if the deformation of the connecting springs vanishes. To fulfill zero spring deformation, we newly introduce a unique mechanism that harnesses additional spin motion to the lighter mass m; the connecting springs can have no deformation even if the longitudinal motions of M and m are the same as those in the original system. The unit cell having the spin-harnessed metamaterial is sketched in figure 1(b). Due to the linkage mechanisms attached to the lighter mass m and the spring k, m is allowed to spin about its center. To couple the additional spin motion with the longitudinal motion of m, two skew-symmetrically installed rigid links are inserted between m and k. To allow the links to rotate freely, pinned joints are employed for connection. As shown in figure 1(b), the mass m of the spin-harnessed metamaterial rotates without longitudinal motion when two adjacent masses M move along the opposite longitudinal directions at ω_L. Because of the rotation, the connecting springs remain undeformed, making ω_L (nearly) zero and realizing a Bragg gap at extremely low frequencies.

It is worth mentioning that there have been some attempts to utilize rotational motion to achieve special elastic metamaterials. For instance, chiral elastic metamaterials [18, 30, 31] utilizing the rotational motion were concerned with the realization of negative elastic parameters. Unlike in these studies, our mechanism incorporates the rotational motion to form a zero-frequency Bragg gap for general periodic systems, which has not been realized or studied previously. The idea of inertia amplification has been studied [32–34] to realize broad stop bands at low frequencies, but their physical origin is different from the Bragg gap considered here. The methods to achieve a very low frequency Bragg gap in a system of granular crystals [35–37] appear hard to be used for general periodic systems.

This work proposes a new mechanism to form a zero-frequency Bragg gap in a general periodic system by using spin-harnessed metamaterials. The validity of the proposed mechanism is checked both numerically and experimentally. Considering the importance of the zero-frequency stop band in various vibration applications, the proposed mechanism is expected to open a new way in various broad-band low frequency vibration devices.

This paper is organized as follows. In section 2, a new mechanism of spin-harnessed metamaterial will be introduced. In section 3, numerical and experimental validation of the proposed mechanism will be given. Conclusions are drawn in section 4.

2. Mechanism of spin-harnessed metamaterial

We begin with the theoretical investigation of the spring deformation as well as the actual motion of a mass–spring system allowing the spin motion of mass m; the corresponding model is illustrated in figure 2(a). For the analysis, all masses are assumed to move only along the x axis but the additional spin motion is allowed in the lighter mass m. To describe the wave physics of the resulting spin-harnessed metamaterial system, we employ the general approach to identify the effective mass and stiffness of a target system by comparing its wave equations with those in a general monatomic lattice. In this section, the involved physics of the spin-harnessed metamaterial system will be explained after the effective parameters of the spin-harnessed metamaterial shown in figure 2(a) are defined first.

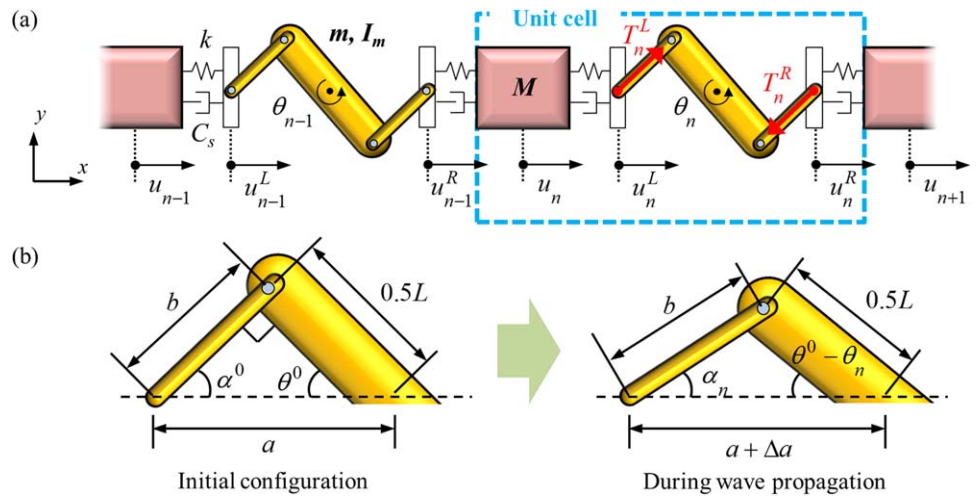

Figure 2. (a) Mass–spring system of the spin-harnessed metamaterial and (b) the undeformed and deformed configurations of the spinning mass during longitudinal wave propagation.

2.1. Derivation of dispersion equation and effective parameters.

At the initial configuration, the spinning mass is assumed to make an angle of θ^0 with respect to the x-axis as in figure 2(b). In addition, the rigid link connecting the lighter mass m and the spring k and damper C_S is assumed to be perpendicular to the mass m. From the geometry of the initial configuration shown in the left figure of figure 2(b), the following equation can be derived:

$$b^2 = a^2 + \left(\frac{1}{2}L\right)^2 - aL\cos\theta^0 = a^2 + \left(\frac{1}{2}L\right)^2 - aL\sin\alpha^0, \tag{1}$$

where α^0 is defined as $\alpha^0 = \pi/2 - \theta^0$. When the mass m spins, θ^0 and a are changed accordingly. Even if a is varied by Δa as the result of the angle change, as illustrated in figure 2(b), the following relation must hold:

$$\begin{aligned} b^2 &= (a+\Delta a)^2 + \left(\frac{1}{2}L\right)^2 - (a+\Delta a)L\cos(\theta^0 - \theta_n) \\ &= (a+\Delta a)^2 + \left(\frac{1}{2}L\right)^2 - (a+\Delta a)L\sin(\alpha^0 + \theta_n). \end{aligned} \tag{2}$$

Combining equations (1) and (2) yields

$$a^2 + \left(\frac{1}{2}L\right)^2 - aL\sin\alpha^0 = (a+\Delta a)^2 + \left(\frac{1}{2}L\right)^2 - (a+\Delta a)L\sin(\alpha^0 + \theta_n), \tag{3}$$

which can be re-written as

$$aL[\sin(\alpha^0 + \theta_n) - \sin\alpha^0] = 2a\Delta a + \Delta a^2 - \Delta aL\sin(\alpha^0 + \theta_n), \tag{4}$$

or

$$2aL\cos(\alpha^0 + \theta_n/2)\sin(\theta_n/2) = 2a\Delta a + \Delta a^2 - \Delta aL\sin(\alpha^0 + \theta_n). \tag{5}$$

The symbol θ_n denotes the rotation angle of the nth spinning (or lighter) mass as in figure 2(a). If the rotation angle of the spinning mass is sufficiently small, linear approximation is possible. In this case, one can assume that $\cos(\alpha^0 + \theta_n/2) \sim \cos\alpha^0$, $\sin(\theta_n/2) \sim \theta_n/2$, $\sin(\alpha^0 + \theta_n) \sim \sin\alpha^0$ and $\Delta a^2 \sim 0$. With these approximations, equation (5) can be reduced to

$$\theta_n aL\cos\alpha^0 = \Delta a(2a - L\sin\alpha^0). \tag{6}$$

Because the spinning mass and the attached links are skew-symmetrically configured, one can show that $\Delta a = (u_n^R - u_n^L)/2$, where u_n^L and u_n^R shown in figure 2(a) denote the longitudinal displacements at the left and right sides of the pinned links connected to the spinning mass m, respectively. As a result, one can obtain the following equation which relates θ_n to u_n^R and u_n^L as

$$\theta_n = \frac{(2a - L\sin\alpha^0)}{aL\cos\alpha^0}\Delta a = \frac{(2a - L\sin\alpha^0)}{2aL\cos\alpha^0}(u_n^R - u_n^L) \equiv F(u_n^R - u_n^L), \tag{7}$$

where the parameter F is defined as $F = (2a - L\sin\alpha^0)/2aL\cos\alpha^0$. The geometric relation in equation (7) will be used in deriving the equation of motion.

In the nth unit cell consisting of the larger mass M and the spinning lighter mass m, the following equations of motion can be derived:

- for the mass M:

$$M\frac{\mathrm{d}^2u_n}{\mathrm{d}t^2} = k(u_{n-1}^R + u_n^L - 2u_n) + C_s\frac{\mathrm{d}}{\mathrm{d}t}(u_{n-1}^R + u_n^L - 2u_n). \tag{8a}$$

- for the spinning mass m:

$$\text{longitudinal motion: } (T_n^L - T_n^R)\cos\alpha^0 = m\frac{\mathrm{d}^2}{\mathrm{d}t^2}\left(\frac{u_n^L + u_n^R}{2}\right), \tag{8b}$$

$$\text{spinning motion } -\frac{1}{2}L(T_n^L + T_n^R) = I_m\frac{\mathrm{d}^2\theta_n}{\mathrm{d}t^2}, \tag{8c}$$

while I_m is the rotational inertia of the spinning mass and T_n^L and T_n^R are the forces acting through the left and right links. Their positive directions are indicated in figure 2(a). Also, $\cos\alpha_n \sim \cos\alpha^0$ is assumed since the rotation angle of the spinning mass is sufficiently small. (Note that α_n is the angle between the rigid link and the x-axis during wave propagation, as shown in figure 2(b).) Since the connecting links are rigid, T_n^L and T_n^R can be expressed in terms of the spring and damping forces as

$$T_n^L\cos\alpha^0 = k(u_n - u_n^L) + C_s\frac{\mathrm{d}}{\mathrm{d}t}(u_n - u_n^L), \tag{9a}$$

$$T_n^R\cos\alpha^0 = k(u_n^R - u_{n+1}) + C_s\frac{\mathrm{d}}{\mathrm{d}t}(u_n^R - u_{n+1}). \tag{9b}$$

In equation (9), only the x-directional components of T_n^L and T_n^R are considered because the left and right sides of the spinning mass are made to move along the x direction only. This constraint produces the constraint reaction forces in the y direction at the hinge joints where u_n^L and u_n^R are measured and these forces counterbalance the angular momentum of the spinning mass m.

For time-harmonic motion of angular frequency ω, equations (8) and (9) can be re-written as

$$-\omega^2Mu_n = \tilde{k}(u_{n-1}^R + u_n^L - 2u_n), \tag{10a}$$

$$T_n^L - T_n^R = -\frac{m\omega^2}{2\cos\alpha^0}(u_n^L + u_n^R), \tag{10b}$$

$$T_n^L + T_n^R = 2\frac{I_m}{L}\omega^2\theta_n, \tag{10c}$$

$$T_n^L\cos\alpha^0 = \tilde{k}(u_n - u_n^L), \tag{10d}$$

$$T_n^R\cos\alpha^0 = \tilde{k}(u_n^R - u_{n+1}), \tag{10e}$$

where $\partial/\partial t = \mathrm{i}\omega$ is used. In equation (10), the complex-valued $\tilde{k}$ is defined as $\tilde{k} = k + \mathrm{i}\omega C_s$. Substituting equation (7) into equation (10c) yields

$$T_n^L + T_n^R = 2\frac{I_mF}{L}\omega^2(u_n^R - u_n^L). \tag{10f}$$

If equations (10b) and (10f) are combined, the following equation can be obtained

$$T_n^L = \left(\frac{I_mF}{L} - \frac{m}{4\cos\alpha^0}\right)\omega^2u_n^R - \left(\frac{I_mF}{L} + \frac{m}{4\cos\alpha^0}\right)\omega^2u_n^L = Au_n^R - Bu_n^L, \tag{11a}$$

$$T_n^R = \left(\frac{I_mF}{L} + \frac{m}{4\cos\alpha^0}\right)\omega^2u_n^R - \left(\frac{I_mF}{L} - \frac{m}{4\cos\alpha^0}\right)\omega^2u_n^L = Bu_n^R - Au_n^L, \tag{11b}$$

where

$$A = \frac{\omega^2I_mF}{L} - \frac{\omega^2m}{4\cos\alpha^0}, \tag{11c}$$

$$B = \frac{\omega^2I_mF}{L} + \frac{\omega^2m}{4\cos\alpha^0}, \tag{11d}$$

If the variables u_n^R and u_n^L are eliminated, one can derive an equation involving the variable u_n only, so that the effective parameters can be defined. To express $(u_n^R,\ u_n^L)$ in terms of u_n, equations (11a), (11b) and equations (10d), (10e) are combined as

$$Au_n^R - Bu_n^L = \frac{\tilde{k}}{\cos\alpha^0}(u_n - u_n^L), \tag{12a}$$

$$Bu_n^R - Au_n^L = \frac{\tilde{k}}{\cos\alpha^0}(u_n^R - u_{n+1}), \tag{12b}$$

which can be equivalently expressed in matrix form as

$$\begin{bmatrix} u_n \\ u_{n+1} \end{bmatrix} = \begin{bmatrix} 1 - B\cos\alpha^0/\tilde{k} & A\cos\alpha^0/\tilde{k} \\ A\cos\alpha^0/\tilde{k} & 1 - B\cos\alpha^0/\tilde{k} \end{bmatrix} \begin{bmatrix} u_n^L \\ u_n^R \end{bmatrix} = \tilde{W} \begin{bmatrix} u_n^L \\ u_n^R \end{bmatrix}, \tag{13a}$$

$$\tilde{W} = \begin{bmatrix} 1 - B\cos\alpha^0/\tilde{k} & A\cos\alpha^0/\tilde{k} \\ A\cos\alpha^0/\tilde{k} & 1 - B\cos\alpha^0/\tilde{k} \end{bmatrix}. \tag{13b}$$

From equation (13*a*), one can derive

$$\begin{bmatrix} u_n^L \\ u_n^R \end{bmatrix} = \frac{1}{\det\tilde{W}} \begin{bmatrix} 1 - B\cos\alpha^0/\tilde{k} & -A\cos\alpha^0/\tilde{k} \\ -A\cos\alpha^0/\tilde{k} & 1 - B\cos\alpha^0/\tilde{k} \end{bmatrix} \begin{bmatrix} u_n \\ u_{n+1} \end{bmatrix}. \tag{13c}$$

Finally, u_{n-1}^R and u_n^L can be explicitly expressed in terms of $(u_n,\ u_{n+1})$,

$$u_{n-1}^R = \frac{1}{\det\tilde{W}}\left(-\frac{A\cos\alpha^0}{\tilde{k}}\right)u_{n-1} + \frac{1}{\det\tilde{W}}\left(1 - \frac{B\cos\alpha^0}{\tilde{k}}\right)u_n, \tag{14a}$$

$$u_n^L = \frac{1}{\det\tilde{W}}\left(1 - \frac{B\cos\alpha^0}{\tilde{k}}\right)u_n + \frac{1}{\det\tilde{W}}\left(-\frac{A\cos\alpha^0}{\tilde{k}}\right)u_{n+1}. \tag{14b}$$

Substituting equations (14*a*), (14*b*) to equation (10*a*) yields

$$-M\omega^2 u_n = -\frac{A\cos\alpha^0}{\det\tilde{W}}(u_{n+1} + u_{n-1} - 2u_n) - p\cdot u_n, \tag{15a}$$

$$p = 2\tilde{k} - \frac{1}{\det\tilde{W}}(2\tilde{k} - 2A\cos\alpha^0 - 2B\cos\alpha^0). \tag{15b}$$

To obtain the dispersion equation in the periodic system, the Floquet–Bloch condition is used as $u_{n+1} = u_n\exp(-\mathrm{i}qD)$ where q and D are the wavevector and periodicity, respectively [29]. Then, equation (15) is reduced to

$$-\left(M - \frac{p}{\omega^2}\right)\omega^2 = -\frac{A\cos\alpha^0}{\det\tilde{W}}(\exp(-\mathrm{i}qD) + \exp(\mathrm{i}qD) - 2)$$

$$= -4\frac{A\cos\alpha^0}{\det\tilde{W}}\sin^2\frac{qD}{2}, \tag{16a}$$

$$p = 2\tilde{k} - \frac{1}{\det\tilde{W}}(2\tilde{k} - 2A\cos\alpha^0 - 2B\cos\alpha^0), \tag{16b}$$

$$\tilde{W} = \begin{bmatrix} 1 - B\cos\alpha^0/\tilde{k} & A\cos\alpha^0/\tilde{k} \\ A\cos\alpha^0/\tilde{k} & 1 - B\cos\alpha^0/\tilde{k} \end{bmatrix}, \tag{16c}$$

$$A = \frac{\omega^2 I_m F}{L} - \frac{\omega^2 m}{4\cos\alpha^0}, \tag{16d}$$

$$B = \frac{\omega^2 I_m F}{L} + \frac{\omega^2 m}{4\cos\alpha^0}, \tag{16e}$$

$$F = (2a - L\sin\alpha^0)/2aL\cos\alpha^0, \tag{16f}$$

$$\tilde{k} = k + \mathrm{i}\omega C_s. \tag{16g}$$

If equation (16*a*) is viewed as the dispersion relation for a monatomic mass–spring system, it can be re-written with the effective mass and stiffness as [29]

$$M_{\mathrm{eff}}\omega^2 = 4K_{\mathrm{eff}}\sin^2(qD/2), \tag{17a}$$

where the effective mass and stiffness parameters for the spin-harnessed metamaterial are defined as

$$M_{\mathrm{eff}} = M - \frac{p}{\omega^2}, \tag{17b}$$

$$K_{\mathrm{eff}} = -\frac{A\cos\alpha^0}{\det\tilde{W}}. \tag{17c}$$

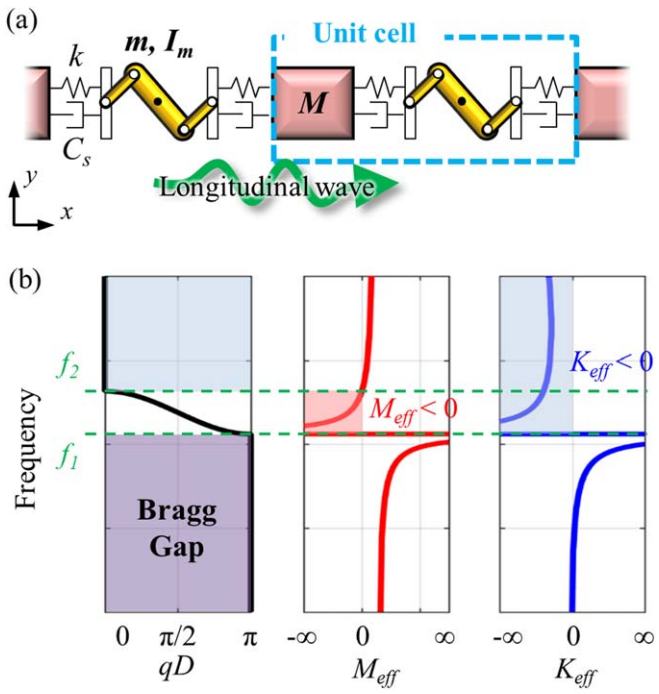

Figure 3. (a) Mass–spring system of the spin-harnessed metamaterial and (b) the dispersion curve, effective mass and spring stiffness of the spin-harnessed metamaterial.

2.2. Wave physics of zero-frequency Bragg gap

Figure 3 plots the dispersion curve, the effective mass M_{eff} and stiffness K_{eff} calculated by equation (17) at various frequencies. Note that the detailed values of the parameters used to plot figure 3, such as M or m, will be given in section 3. However, the wave physics explained in this section generally hold. Also, the damping coefficient C_s appearing in the actual system was not considered to explain the physics of the spin-harnessed system better. The dispersion curve plotted in figure 3(b) shows that a stop band is formed from 0 Hz to frequency $f_1 = \sqrt{2k/m}/2\pi$ Hz. To confirm that the formed stop band is a Bragg gap, *we argue that* (1) *the real value of the wavevector q is π/D and that* (2) *both of the effective mass and stiffness are positive in this frequency range*; see figure 3(b) [29]. It is remarked that the Bragg gap occurs if the left term in equation (17*a*), $M_{\text{eff}}\omega^2$, becomes larger than the right term, $4K_{\text{eff}}$. In this case, there exists no real-valued q that can satisfy the wave dispersion equation in equation (17*a*) [29]. Therefore, both the effective mass and stiffness should be positive in the Bragg gap; if either the effective mass M_{eff} or stiffness K_{eff} were negative, the formed stop band would not be a Bragg gap. (This type of band gaps has been actively studied using resonance-based metamaterials because they can yield negative parameters for the formation of a stop band.) In figure 3(b), it can be clearly observed that K_{eff} is extremely small for frequencies between 0 Hz and f_1 Hz and thereby $M_{\text{eff}}\omega^2$ is larger than $4K_{\text{eff}}$. Because $M_{\text{eff}} > 0, K_{\text{eff}} > 0$ and qD is complex-valued between 0 Hz and f_1 Hz, the formed stop band in the frequency range can be clearly identified as a Bragg gap starting from $\omega_L = 0$. Note that $K_{\text{eff}} = 0$ at $f = 0$ Hz in the proposed mass–spring system, which indicates that the spinning mass m at $f = 0$ Hz will simply rotate and do not transfer any longitudinal force along the x direction when an external force is applied at the left end of the spin-harnessed metamaterial system. However, zero transmission of the longitudinal force could cause a structural stability issue in practical applications; see the appendix for more details about the stability issue.

In the pass band between $f_1 = \sqrt{2k/m}/2\pi$ Hz and $f_2 = \sqrt{2k(m+M)/mM}/2\pi$ Hz, the wave speed is negative because the effective mass and stiffness are simultaneously negative as evidenced by figure 3(b). The negative wave speed is expected because the dispersion curve between f_1 and f_2 corresponds to the optical branch of a general diatomic mass–spring system. The notion of effective parameters may not be useful for an optical branch because the frequency range of a typical optical branch usually exceeds the homogenization limit. If an optical branch is formed at sufficiently low frequencies below the homogenization limit, however, the notion of effective parameters can be useful. As proven in the previous works on the coiling up space [38–40], the optical branch appearing below the homogenization limit yields double negativity, which can be clearly seen in figure 3(b).

Finally, we examine the wave behavior of the spin-harnessed metamaterial system above f_2 Hz. In this frequency range, a broad stop band is formed because only the effective stiffness is negative. This behavior can also be predicted because a semi-infinitely wide stop band is formed after the optical branch. In the actual spin-

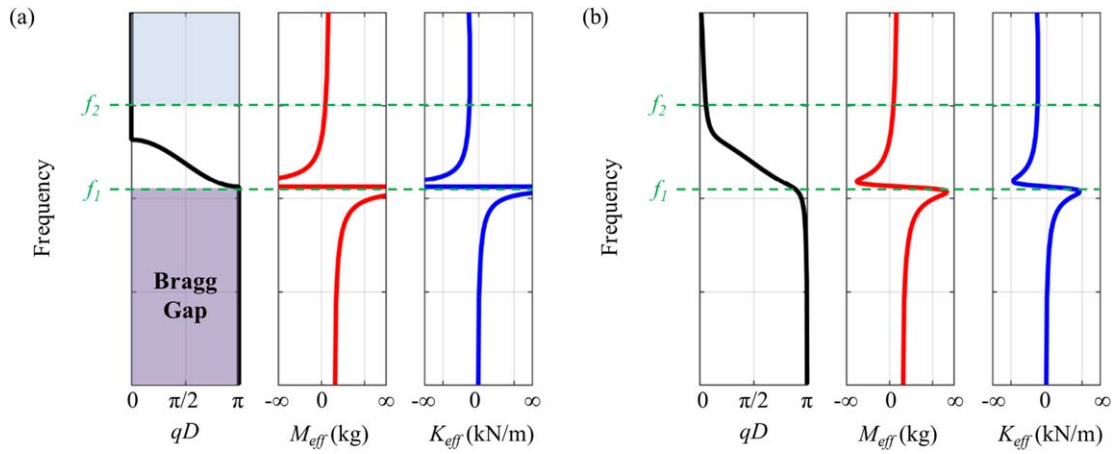

Figure 4. The dispersion curve, effective mass and spring coefficients for (a) the lossless case and (b) the lossy case with the damping coefficient of $C_S = 0.8$.

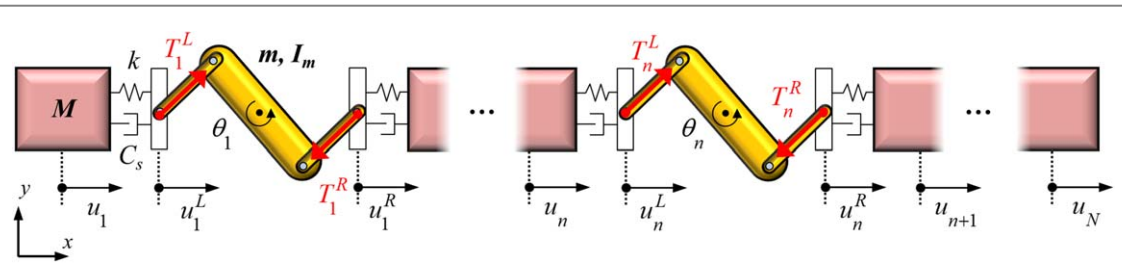

Figure 5. Mass–spring system of the finite spin-harnessed metamaterial.

harnessed metamaterial system, however, there can be another wave branch because it has continuum characteristics, which cannot be fully described by the theoretic investigation based on the discrete mass–spring system.

In the previous investigations, the dispersion curve and the effective parameters were evaluated for the lossless case. In the actual spin-harnessed metamaterial, however, damping may not be ignored. Therefore, the effect of the damping on the zero-frequency Bragg gap is also studied. Figure 4 plots the dispersion curve and the effective parameters for the undamped and damped case. Note that only the real values are plotted in the figures. For the undamped case, the effective parameters are all real-valued over all frequencies. For the damped case, however, the effective parameters are complex-valued because of damping, but the stop band frequencies for the damped case are not much altered for those of the undamped case. Therefore, the dispersion analysis using the results for the undamped case can be used to predict wave behavior in the damped case.

The analysis in this section shows that if an additional spinning motion is added to the lighter mass, the Bragg gap starting from zero frequency can be achieved. Because the Bragg gap is usually broader than the stop band achieved by the internal resonance phenomena, the stop band formed by using the proposed spin-harnessed metamaterial can form a broad band gap starting from zero frequency. For instance, one can realize an extremely broad stop band from 0 Hz to $f_1 = \sqrt{2k/m}/2\pi$ Hz by increasing f_1 with adjusted k and m values.

2.3. Wave transmission for the finite spin-harnessed metamaterial system

In the previous section, the spin-harnessed metamaterial of infinite length is considered. In actual metamaterial realization, however, the metamaterial should be finite. Therefore, we should check whether the Bragg gap is actually formed in a low-frequency range for the case of the finite-length spin-harnessed metamaterial.

Figure 5 shows the finite version of mass–spring system shown in figure 2; the system consists of N number of mass M. In this case, the resulting system consists of $N-1$ unit cells and the transmission ratio can be defined as $|u_N/u_1|$. To derive it analytically, the transfer matrix approach will be employed. First, equations (8*a*)–(8*c*) and (9*a*), (9*b*) are written for each unit cell as:

- for the 1st unit cell

$$-\omega^2 M u_1 = \tilde{k}(u_1^L - u_1), \tag{18a}$$

$$T_1^L \cos\alpha^0 = \tilde{k}(u_1 - u_1^L), \tag{18b}$$

$$(T_1^L - T_1^R)\cos\alpha^0 = -m\omega^2\left(\frac{u_1^L + u_1^R}{2}\right), \tag{18c}$$

$$-\frac{1}{2}L(T_1^L + T_1^R) = -I_m\omega^2\theta_1, \tag{18d}$$

$$T_1^R \cos\alpha^0 = \tilde{k}(u_1^R - u_2). \tag{18e}$$

- for the nth unit cell ($2 \leqslant n \leqslant N-1$)

$$-\omega^2 M u_n = \tilde{k}(u_n^L + u_{n-1}^R - 2u_n), \tag{19a}$$

$$T_n^L \cos\alpha^0 = \tilde{k}(u_n - u_n^L), \tag{19b}$$

$$(T_n^L - T_n^R)\cos\alpha^0 = -m\omega^2\left(\frac{u_n^L + u_n^R}{2}\right), \tag{19c}$$

$$-\frac{1}{2}L(T_n^L + T_n^R) = -I_m\omega^2\theta_n, \tag{19d}$$

$$T_n^R \cos\alpha^0 = \tilde{k}(u_n^R - u_{n+1}). \tag{19e}$$

- for the final mass M (Nth mass)

$$-\omega^2 M u_N = \tilde{k}(u_{N-1}^R - u_N). \tag{20}$$

If u_n^R and u_n^L are expressed in terms of u_n by using equations (14*a*) and (14*b*), we have

- for the 1st unit cell

$$u_1^L = \frac{1}{\det\tilde{W}}\left(1 - \frac{B\cos\alpha^0}{\tilde{k}}\right)u_1 + \frac{1}{\det\tilde{W}}\left(-\frac{A\cos\alpha^0}{\tilde{k}}\right)u_2. \tag{21}$$

- for the nth unit cell ($2 \leqslant n \leqslant N-1$)

$$u_{n-1}^R = \frac{1}{\det\tilde{W}}\left(-\frac{A\cos\alpha^0}{\tilde{k}}\right)u_{n-1} + \frac{1}{\det\tilde{W}}\left(1 - \frac{B\cos\alpha^0}{\tilde{k}}\right)u_n, \tag{22a}$$

$$u_n^L = \frac{1}{\det\tilde{W}}\left(1 - \frac{B\cos\alpha^0}{\tilde{k}}\right)u_n + \frac{1}{\det\tilde{W}}\left(-\frac{A\cos\alpha^0}{\tilde{k}}\right)u_{n+1}. \tag{22b}$$

- and for the final mass M (the N^{th} mass),

$$u_{N-1}^R = \frac{1}{\det\tilde{W}}\left(-\frac{A\cos\alpha^0}{\tilde{k}}\right)u_{N-1} + \frac{1}{\det\tilde{W}}\left(1 - \frac{B\cos\alpha^0}{\tilde{k}}\right)u_N. \tag{23}$$

Substituting equations (21)–(23) into equations (18*a*), (19*a*), (20) yield:

- for the 1st unit cell

$$-\omega^2 M u_1 = \left(-\tilde{k} + \frac{\tilde{k}}{\det\tilde{W}} - \frac{B\cos\alpha^0}{\det\tilde{W}}\right)u_1 - \frac{A\cos\alpha^0}{\det\tilde{W}}u_2. \tag{24}$$

- for the nth unit cell ($2 \leqslant n \leqslant N-1$)

$$-\omega^2 M u_n = \left(-2\tilde{k} + \frac{2\tilde{k}}{\det\tilde{W}} - \frac{2B\cos\alpha^0}{\det\tilde{W}}\right)u_n - \frac{A\cos\alpha^0}{\det\tilde{W}}(u_{n+1} + u_{n-1}). \tag{25}$$

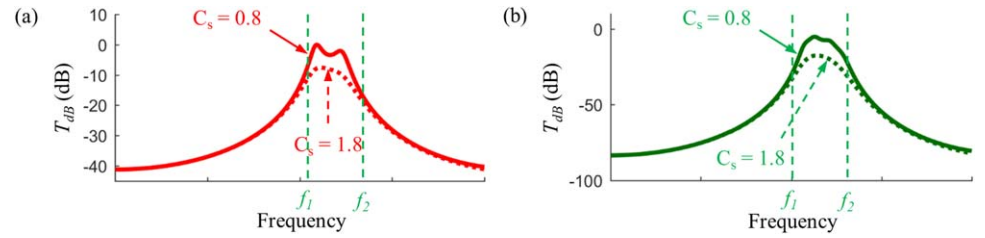

Figure 6. The wave transmission calculated analytically for damping coefficients $C_S = 0.8$ and $C_S = 0.8$ for the metamaterial systems consisting of (a) 2 unit cells and (b) 4 unit cells.

- for the final mass M (Nth mass)

$$-\omega^2 M u_N = \left(-\tilde{k} + \frac{\tilde{k}}{\det\tilde{W}} - \frac{B\cos\alpha^0}{\det\tilde{W}}\right)u_N + -\frac{A\cos\alpha^0}{\det\tilde{W}}u_{N-1}. \tag{26}$$

If a symbol denoting the displacement ratio $U_{n-1}^n = u_n/u_{n-1}$ is introduced, it will be more convenient to obtain the transmission ratio. To this end, equation (25) is re-written as

$$\left(2\tilde{k} - \frac{2\tilde{k}}{\det\tilde{W}} + \frac{2B\cos\alpha^0}{\det\tilde{W}} - \omega^2 M\right)u_n = -\frac{A\cos\alpha^0}{\det\tilde{W}}(u_{n+1} + u_{n-1}). \tag{27}$$

Dividing both sides of equation (27) by u_{n-1} yields

$$\left(2\tilde{k} - \frac{2\tilde{k}}{\det\tilde{W}} + \frac{2B\cos\alpha^0}{\det\tilde{W}} - \omega^2 M\right)\frac{u_n}{u_{n-1}} = -\frac{A\cos\alpha^0}{\det\tilde{W}}\left(\frac{u_{n+1}}{u_{n-1}} + 1\right). \tag{28}$$

Using the relation $u_{n+1}/u_{n-1} = u_{n+1}/u_n \times u_n/u_{n-1} = U_n^{n+1}U_{n-1}^n$, the following equation can be obtained:

$$\left(2\tilde{k} - \frac{2\tilde{k}}{\det\tilde{W}} + \frac{2B\cos\alpha^0}{\det\tilde{W}} - \omega^2 M + \frac{A\cos\alpha^0}{\det\tilde{W}}U_n^{n+1}\right)U_{n-1}^n = -\frac{A\cos\alpha^0}{\det\tilde{W}}. \tag{29}$$

From equation (29), one can show that U_{n-1}^n is related to U_n^{n+1} as

$$U_{n-1}^n = -\frac{A\cos\alpha^0}{2\tilde{k}\det\tilde{W} - 2\tilde{k} + 2B\cos\alpha^0 - \omega^2 M\det\tilde{W} + A\cos\alpha^0 U_n^{n+1}}. \tag{30}$$

Equation (30) suggests that U_n^{n+1} (or U_{n-2}^{n-1}) is needed to calculate U_{n-1}^n. Accordingly, either U_1^2 or U_{N-1}^N should be known, in order to calculate $|u_N/u_1|$ by using the recurrence formula. Here, we will calculate U_{N-1}^N explicitly to start the recurrence formula. (Obviously, one can proceed to use the recurrence formula when U_1^2 is known.)

By rewriting equation (26) as

$$\left(\tilde{k} - \frac{\tilde{k}}{\det\tilde{W}} + \frac{B\cos\alpha^0}{\det\tilde{W}} - \omega^2 M\right)u_N = -\frac{A\cos\alpha^0}{\det\tilde{W}}u_{N-1}, \tag{31}$$

one can obtain the explicit formula for U_{N-1}^N as

$$U_{N-1}^N = -\frac{A\cos\alpha^0}{\tilde{k}\det\tilde{W} - \tilde{k} + B\cos\alpha^0 - \omega^2 M\det\tilde{W}}. \tag{32}$$

As can be seen in equation (32), U_{N-1}^N is a function of the known parameters only. Therefore, one can calculate U_{N-1}^N from equation (32), and by repeating the same process, all other terms (U_{N-2}^{N-1} U_{N-3}^{N-2}, …, U_2^3 and U_1^2) can be calculated from equation (30). Finally, the wave transmission ratio can be calculated analytically as

$$\left|\frac{u_N}{u_1}\right| = \left|\frac{u_N}{u_{N-1}}\right|\left|\frac{u_{N-1}}{u_{N-2}}\right|\ldots\left|\frac{u_3}{u_2}\right|\left|\frac{u_2}{u_1}\right| = |U_{N-1}^N||U_{N-2}^{N-1}|\ldots|U_2^3||U_1^2| = \prod_{i=2}^{N}|U_{n-1}^n|, \tag{33}$$

or, in decibel scale

$$T_{\mathrm{dB}}^{\mathrm{Theory}} = 20\log_{10}\left|\frac{u_2}{u_1}\right|\left|\frac{u_3}{u_2}\right|\ldots\left|\frac{u_N}{u_{N-1}}\right| = 20\log_{10}\left(\prod_{i=2}^{N}|U_{n-1}^n|\right). \tag{34}$$

Figure 6 shows the numerically calculated wave transmission $T_{\mathrm{dB}}^{\mathrm{Theory}}$ for the mass–spring system consisting of 2 and 4 unit cells. Here, the same unit cell considered in figure 3 is used in the analytic calculation, i.e., the metamaterial is shown to have a Bragg gap from 0 Hz to f_1 Hz, pass band from f_1 Hz to f_2 Hz and band gap above f_2 Hz. It can be seen that the finite metamaterial system also exhibits same wave characteristics predicted by the infinite metamaterial system; very low wave transmission from 0 Hz to f_1 Hz and above f_2 Hz is observed for both

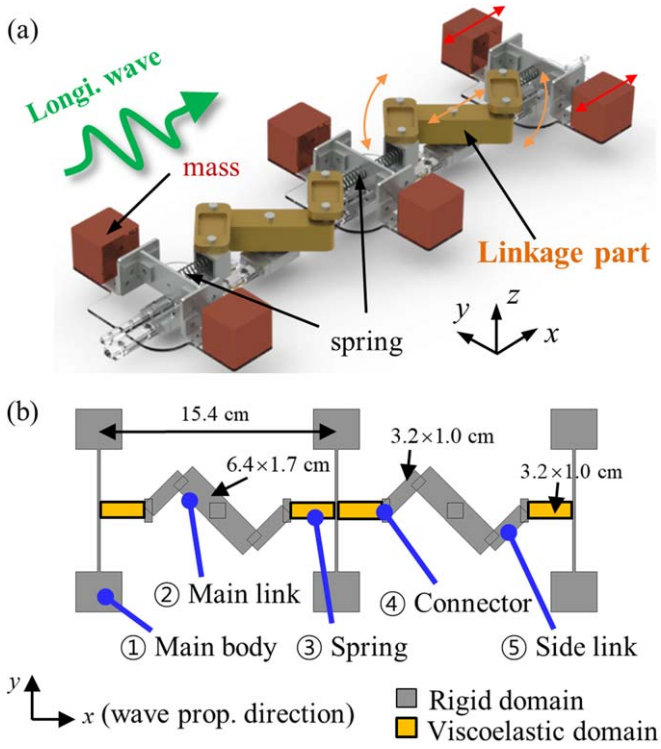

Figure 7. (a) Schematics of the actual spin-harnessed metamaterial considered in this work and (b) the detailed components of the actual metamaterial.

2 and 4 unit cell cases, and relatively high wave transmission can be seen from f_1 Hz to f_2 Hz. This shows that the zero-frequency Bragg gap from 0 Hz to f_1 Hz can be effectively formed with finite metamaterial structures.

Furthermore, figure 6 also shows the wave transmission change for various damping coefficient. As can be seen in figure 6, the damping coefficient value affects the vibration transmission mainly in the pass bands, not in the stop bands. This is due to the fact that the effect of damping is different depending on the frequency range. In the pass band, waves can be well transmitted through each unit cell and thus the damping effect can take place over the whole unit cells. In the stop bands, however, waves cannot propagate through the system so that wave energy is mostly confined near the directly actuated unit cell. Accordingly, the damping effect influences the system very locally near the excitation point. This results also suggest that the formation of the zero-frequency Bragg gap which was validated with undamped case can also be extended to the damped case.

3. Numerical and experimental validation

To validate our idea, a new spin-harnessed metamaterial is designed and numerical and experimental investigations are carried out. Among various metamaterials possible from our new mechanism, figure 7(a) shows the actual spin-harnessed metamaterial considered in this work for the numerical and experimental investigation. Since the actual spin-harnessed metamaterial is somewhat complicated, the role of each part is explained.

1. Main body: It acts as a lumped mass M in the mass–spring system. To ensure that it behaves as a rigid body, it is made of steel (SM45C). The motion of the main body corresponds to the displacement u_n of the mass–spring system shown in figure 2.
2. Main link: This part acts as the spinning mass m. It can move along the x-direction and also rotate about its center in the plane. Due to its slender shape, it has not only mass m but also inertia I_m. Due to the same reason in the main body, it is made of steel (SM45C).
3. Spring: It is used to store elastic energy and represents the spring k in the mass–spring system shown in figure 2. Here, a spring with the stiffness value of 2000 N m^{-1} is considered (WL14-35, Misumi).

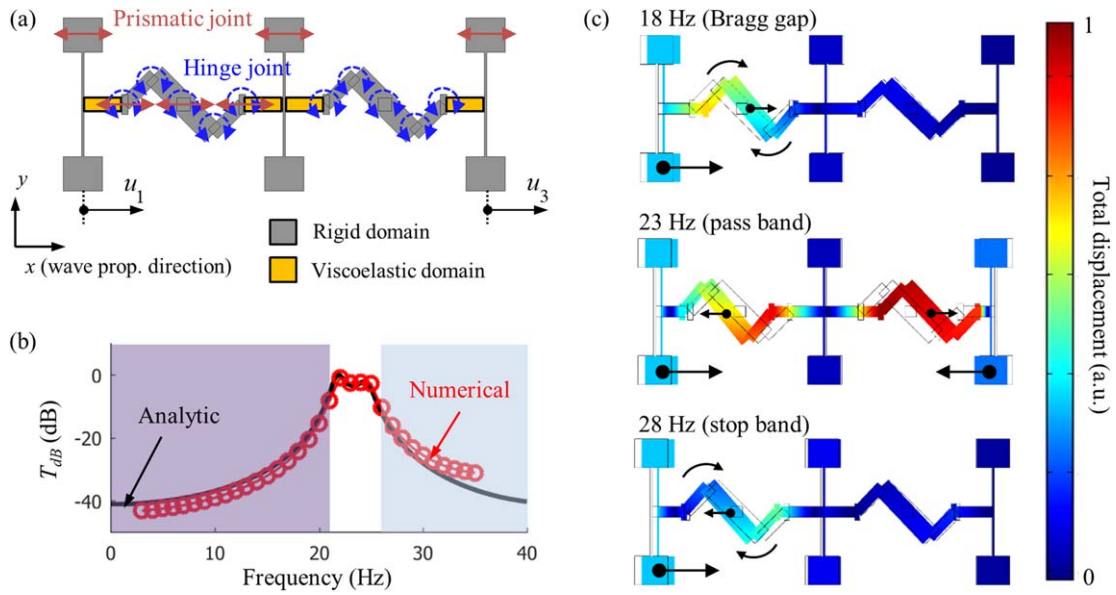

Figure 8. (a) Numerical simulation model of the actual spin-harnessed metamaterial, (b) analytically and numerically calculated wave transmission, (c) wave motions at various actuation frequencies.

4. Connector: This part connects the spring and the linkage part. To minimize the undesirable deformation of the connector, it is made of aluminum (A601) having low density but high stiffness. The movements of the connectors are denoted by u_n^R and u_n^L in the mass–spring system shown in figure 2.

5. Side link: The main role of the side link is to connect the connector and the main link. Because it is made of a light plastic material (MC-nylon), it is assumed to make no contribution to the mass and stiffness of the system.

With the geometric parameters shown in figure 7(b) and the materials given above, the actual spin-harnessed metamaterial can be considered as the mass–spring system in figure 2 with the following parameters;

$$M = 0.4168 \text{ kg}, \tag{35a}$$

$$m = 0.2250 \text{ kg}, \tag{35b}$$

$$I_m = 6945 \text{ cm}^4, \tag{35c}$$

$$k = 2000 \text{ N m}^{-1}, \tag{35d}$$

$$\alpha^0 = 45°, \tag{35e}$$

$$a = 4.5 \text{ cm}, \tag{35f}$$

$$D = 15.4 \text{ cm}. \tag{35g}$$

From our mechanism developed in section 2, the spin-harnessed metamaterial is expected to have a stop band from 0 Hz to $f_1 = \sqrt{2k/m}/2\pi = 21.22$ Hz, a pass band from $f_1 = 21.22$ Hz to $f_2 = \sqrt{2k(m+M)/mM}/2\pi = 26.33$ Hz and a stop band above $f_2 = 26.33$ Hz. Based on the information, the formation of stop and pass bands will be numerically and experimentally checked by measuring the wave transmission defined in equation (34) for the finite spin-harnessed metamaterial system.

3.1. Numerical investigation on the proposed spin-harnessed metamaterial.

Figure 8(a) shows the numerical modeling to simulate the wave transmission. For the numerical simulation, the COMSOL Multibody Dynamics Module was used. Since the main body, main link and side link are significantly stiffer than the spring part, they were modeled as rigid bodies. Also, the spring part was considered as a viscoelastic material having complex-valued Young's modulus to take the damping effect into consideration. To consider the complicated connections in the spin-harnessed metamaterial, two kinds of joint conditions were used; a prismatic joint condition was used to guarantee the one-dimensional motion along the x-direction and a hinge joint was used to allow each part to rotate freely.

For actuation, the first main body was excited at an amplitude of 0.2 mm. Then, vibration analysis (time-harmonic analysis) was carried out at various frequencies. After the simulation was completed, the x directional displacement of the third main body (denoted as u_3) was normalized with respect to that of the first main body

(denoted as u_1). Finally, the wave transmission was calculated as $T_{\mathrm{dB}}^{\mathrm{Simulation}} = 20\log_{10}|u_3/u_1|$. If $u_3 = u_1$, for instance, the transmission is calculated to be 0. Note that since the simulation is based on the vibration simulation, i.e., both the incident and reflected waves exist in the simulation result, u_3 can be larger than u_1 and T_{dB} can be larger than 0.

Figure 8(b) shows the wave transmission calculated by the numerical simulation and by the analytic calculation. Very good agreements can be observed between the two results, justifying our analytic investigation. From the analytic and numerical results, it can be clearly seen that the wave transmission is extremely low at very low frequencies which correspond to the Bragg gap frequencies (below 21.22 Hz). Also, significantly high wave transmission is measured around the frequency range from 21 to 26 Hz, which corresponds to the pass band of the spin-harnessed metamaterial (from 21.22 to 26.33 Hz).

Note that in the COMSOL Multibody Dynamics Module, the geometric nonlinearity (the effect of the angle change in the linkage part) is considered, while our analytic equation was derived based on the linear assumption. The geometric nonlinearity effects can be more significant at high frequencies because the rotational motion of the metamaterial becomes significant. However, two results agree well as shown in figure 8(b), indicating the geometric nonlinearity can be ignored if the magnitude of the actuation displacement is not very large. In addition, the simulation results show that the spin-harnessed metamaterial based on our new mechanism can effectively provide a stop band only with two unit cells.

Figure 8(c) shows the numerical simulation results of the spin-harnessed metamaterial at the frequencies of 18, 23 and 28 Hz. Note that 18 and 28 Hz belong to the stop band, while 23 Hz, to the pass band. At 18 Hz, the first main body moves along the positive x-direction and the main link rotates clockwise. Due to the spinning motion of the main link, almost no longitudinal wave is transmitted through the second mass, resulting in extremely low vibration transmission. This dynamic motion can also explain why the analytically calculated effective stiffness of the spin-harnessed metamaterial becomes almost zero in the frequency belonging to the stop band.

On the other hand, the dynamic motion at 23 Hz is somewhat different from that at 18 Hz. At 23 Hz, the motion of the main link is dominated by the translational motion along the x-direction, rather than the spinning motion as observed at 18 Hz; in the frequency range of the optical branch, the translational movement of the lighter mass becomes significant and due to this translational motion, the longitudinal wave can be transmitted through the system. Accordingly, high wave transmission is observed in the optical frequency range.

At 28 Hz, figure 8(c) shows that the spinning motion dominates the motion of the main link again, preventing the longitudinal wave transmission through the spin-harnessed metamaterial. However, the detailed spinning behavior is different from that observed at 18 Hz. At 18 Hz, both the main body and link move along the positive x-direction but at 28 Hz, the main body moves along the positive x-direction while the main link moves along the negative x-direction. This shows that the motion of the main link at 18 Hz is dominated only by the spinning motion, while at 28 Hz, both the translation and spinning motion dominate the main link.

3.2. Experimental investigation on the proposed spin-harnessed metamaterial.

To experimentally validate the formation of a Bragg gap starting from zero or a very low frequency, the spin-harnessed metamaterial system is fabricated as in figure 9. To ensure dominant longitudinal wave motion along the x direction, the spin-harnessed metamaterial system was installed on a linear motion guide. Note that the spin-harnessed metamaterial is designed to have $f_1 = 21.22$ Hz and $f_2 = 26.33$ Hz.

Based on the fabrication, the detailed experimental setting is shown in figure 9. For the actuation of a longitudinal motion, a vibration shaker (Modal exciter type 4809, Bruel & Kjaer) was connected to the left side of the spin-harnessed metamaterial system shown in figure 9. Sine waves with an amplitude of 2.56 mm at actuation frequencies varying from 3 to 31 Hz were excited and the longitudinal displacement (u_1) of the first heavier mass (M) at the excitation point was recorded. At the right side of the spin-harnessed metamaterial system, the longitudinal displacement (u_3) of the third heavier mass along the x axis was measured by using a laser vibrometer (OFV-551, Polytec).

Figure 10(a) shows the measured displacements u_1 and u_3 at various frequencies. To eliminate noise from the measured signals, measurements were repeated and averaged more than 20 times for each actuation frequency and post-processed with the Fourier transformation as shown in figure 10(b). The measurements were carried out under steady state conditions, implying that the actual experiments were vibration experiments. Using the measured experimental data, the wave transmission ratios $T_{\mathrm{dB}}^{\mathrm{Experiment}} = |u_3|/|u_1|$ were estimated for each frequency. Note that the dispersion curve and effective material parameters cannot be calculated from the current experiments. However, the experimental results can be used to investigate the actual frequency range of the stop band.

Figure 10(c) compares the wave transmission obtained by analytical, numerical, and experimental methods for a wide range of frequencies. To obtain the analytical and numerical results, the damping value of $C_S = 1.8$, estimated from the experimentally measured vibration response, is used. As shown in figure 10(c), the

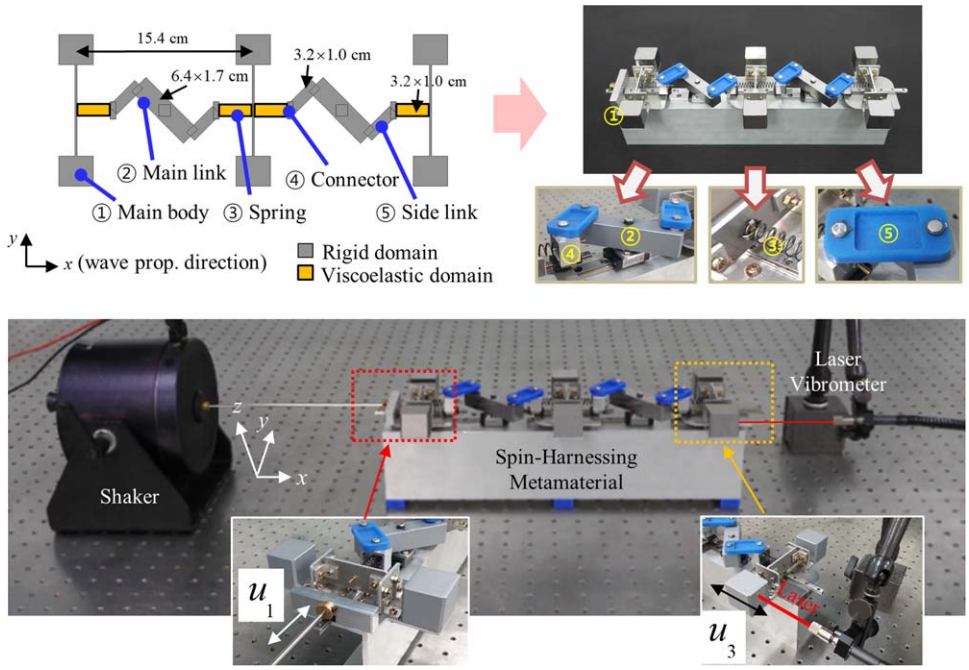

Figure 9. Photo of the fabricated spin-harnessed metamaterial and experimental setup.

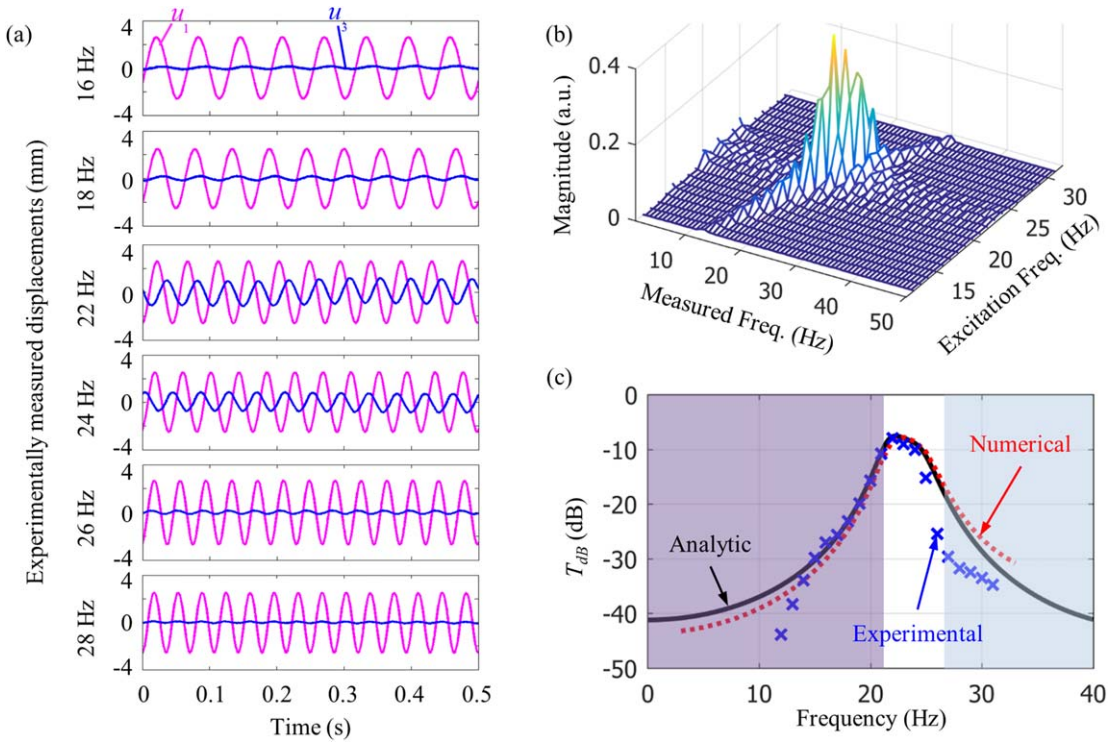

Figure 10. (a) The measured displacements u_1 and u_3 at various frequencies, (b) the Fourier spectra of the measured displacement u_3 for various frequencies and (c) the comparison of the analytical, numerical and experimental wave transmission ratios, $|u_3|/|u_1|$.

transmission ratios calculated by different methods agree well with each other, except at frequencies over 25 Hz. Figure 10(c) clearly shows that relatively low vibration transmission occurs for $0 \leqslant f \leqslant f_1 = 21.22$ Hz and $f_2 = 26.33$ Hz $\leqslant f$ while relatively high transmission occurs between $f_1 = 21.22$ Hz and $f_2 = 26.33$ Hz.

Indeed, the formation of a low-transmission frequency zone below $f_1 = 21.22$ Hz is a clear indication of the formation of a stop band in a very low frequency range.

The discrepancy between the experimental and the numerical/analytical results at frequencies higher than 25 Hz is mainly due to nonlinear effects resulting from large displacement/deformation of the components comprising the spin-harnessed metamaterial system. As the actuation frequency becomes higher (while the magnitude of the input displacement fixed), the increased inertia force causes larger displacement/deformation. In fact, the change in the geometric configuration of the linkage part became so large that the experiment was almost impossible at the frequencies higher than 32 Hz. To check any adverse effect of nonlinear behavior originating from the geometric change in the linkage part at other frequencies, figure 10(b) is prepared. If the nonlinearity is significant, frequency components other than the single excitation frequency would be observed from the measured signal u_3. However, figure 10(b) confirms that the most dominant frequency component in u_3 is the excitation frequency while the magnitudes of other frequency components appearing in u_3 are small compared with that of the excitation frequency component. This validates our linear assumption for analytical dispersion analysis. However, the amplitude of the actuated frequency component was taken from u_3 in calculating the wave transmission.

4. Conclusion

Through this study, we established a new mechanism that can form a Bragg gap starting from zero or a very low frequency. Specifically, we showed that the zero-frequency Bragg gap can be formed if a spin motion is coupled with the main longitudinal wave motion of a lighter mass in a diatomic mass–spring system. Spin motion can be harnessed to the lighter mass m of a diatomic mass–spring system by installing two skew-symmetrically attached linkages to m, making zero elastic deformation in the springs of the system at the lower band-edge frequency of the Bragg gap. The theoretical analysis showed that the lower band-edge frequency becomes zero if the spin motion is properly harnessed. The simulations and actual experiments confirmed that a Brag gap covering 0–21 Hz can be formed by using the spin-harnessed metamaterial system made of a relatively small-period unit cell (15.4 cm).

The proposed mechanism to form a zero- (or low-) frequency Bragg gap is expected to be a new way to make various low-frequency wave controlling devices. Especially, because a traditional mechanism to form a Bragg gap for low-frequency applications would require a large-sized structure, the proposed spin-harnessed metamaterial system could be an alternative to form a broad low-frequency stop band. Besides, the proposed mechanism gives us an insight into a new type of low-frequency vibration isolation devices.

Acknowledgments

This work was supported by the Center for Advanced MetaMaterials (CAMM) funded by the Ministry of Science, ICT and Future Planning as Global Frontier Project (CAMM-2014M3A6B3063711) and by the National Research Foundation of Korea (NRF) grant funded by the Korea government (Nos. 2017R1C1B1004436 and 2016R1A2B3010231).

Appendix

A1. Effect of the initial folding for spin-harnessed metamaterial

Since the spin-harnessed metamaterial has zero stiffness at the static limit, it is unstable and there is a possibility that any nonzero initial force can change the initial configuration of the spinning mass due to the folding, as illustrated in figure A1. In this case, the dynamic characteristics, such as the dispersion curve or the Bragg gap frequencies, may be different from those considered in section 2. Therefore, we will investigate if the effect of the initial folding configuration is significant.

First, consider the initially folded linkage structure shown in the left illustration of figure A1 (b) with the folding configuration parameters $\alpha_{\mathrm{FC}} \neq \alpha^0$, $\theta^0_{\mathrm{FC}} \neq \theta^0$ and $\beta \neq \pi/2$. From the geometry, one can derive the following relation:

$$b^2 = a_{\mathrm{FC}}^2 + \left(\frac{1}{2}L\right)^2 - a_{\mathrm{FC}} L \cos\theta^0_{\mathrm{FC}}. \tag{A1}$$

If the spinning motion changes the length a_{FC} and the angle θ^0_{FC} by Δa and θ_n, respectively, as shown in the right illustration of figure A1(b), the following relation holds

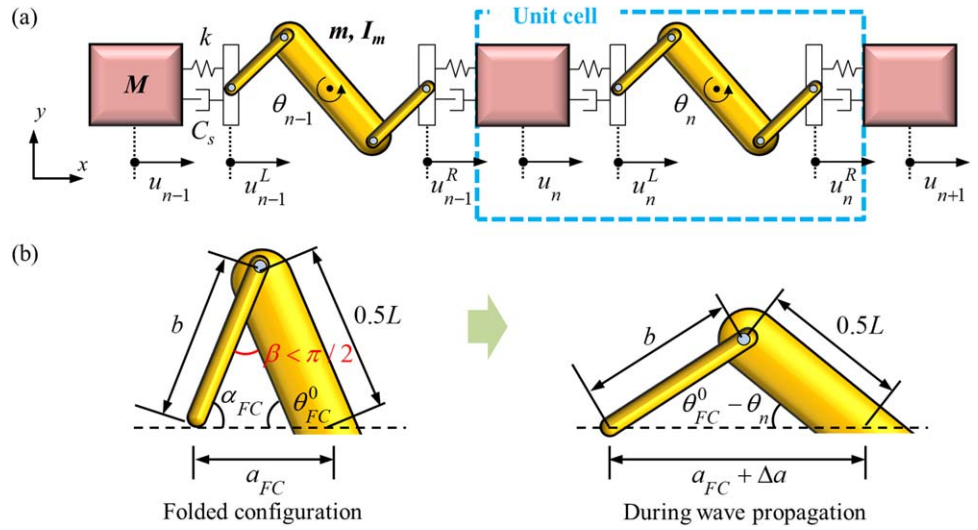

Figure A1. (a) Mass–spring system of the spin-harnessed metamaterial and (b) the geometric change of the linkage mechanism having a different initial folding configuration. The folding configuration is described by α_{FC}, a_{FC} and θ^0_{FC}.

$$b^2 = (a_{\mathrm{FC}} + \Delta a)^2 + \left(\frac{1}{2}L\right)^2 - (a_{\mathrm{FC}} + \Delta a)L\cos(\theta^0_{\mathrm{FC}} - \theta_n). \tag{A2}$$

Combining equations (A1) and (A2) yields

$$a^2_{\mathrm{FC}} + \left(\frac{1}{2}L\right)^2 - a_{\mathrm{FC}}L\cos\theta^0_{\mathrm{FC}} = (a_{\mathrm{FC}} + \Delta a)^2 + \left(\frac{1}{2}L\right)^2 - (a_{\mathrm{FC}} + \Delta a)L\cos(\theta^0_{\mathrm{FC}} - \theta_n). \tag{A3}$$

One can re-write equation (A3) as

$$a_{\mathrm{FC}}L[\cos(\theta^0_{\mathrm{FC}} - \theta_n) - \cos\theta^0_{\mathrm{FC}}] = 2a_{\mathrm{FC}}\Delta a + \Delta a^2 - \Delta aL\cos(\theta^0_{\mathrm{FC}} - \theta_n). \tag{A4}$$

The cosine terms in the left side of equation (A4) can be combined as

$$2a_{\mathrm{FC}}L\cos(\theta^0_{\mathrm{FC}} - \theta_n/2)\sin(\theta_n/2) = 2a_{\mathrm{FC}}\Delta a + \Delta a^2 - \Delta aL\cos(\theta^0_{\mathrm{FC}} - \theta_n). \tag{A5}$$

With the small deformation assumption such that $\Delta a^2 \sim 0$, $\cos(\theta^0_{\mathrm{FC}} - \theta_n/2) \sim \cos\theta^0_{\mathrm{FC}}$ and $\sin(\theta_n/2) \sim \theta_n/2$, equation (A5) reduces to

$$\theta_n a_{\mathrm{FC}}L\cos\theta^0_{\mathrm{FC}} = \Delta a(2a_{\mathrm{FC}} - L\cos\theta^0_{\mathrm{FC}}). \tag{A6}$$

Finally, one can derive the following equation

$$\theta_n = \frac{(2a_{\mathrm{FC}} - L\cos\theta^0_{\mathrm{FC}})}{a_{\mathrm{FC}}L\cos\theta^0_{\mathrm{FC}}}\Delta a = \frac{(2a_{\mathrm{FC}} - L\cos\theta^0_{\mathrm{FC}})}{a_{\mathrm{FC}}L\cos\theta^0_{\mathrm{FC}}}(u^R_n - u^L_n) = F_{\mathrm{FC}}(u^R_n - u^L_n), \tag{A7}$$

where the parameter F_{FC} is defined as $F_{\mathrm{FC}} = (2a_{\mathrm{FC}} - L\cos\theta^0_{\mathrm{FC}})/a_{\mathrm{FC}}L\cos\theta^0_{\mathrm{FC}}$. This equation shows that the effect of the initial folding is that the parameter F is replaced by F_{FC}.

Using the relations derived above, one can derive the equation of motion as

- the mass part M

$$M\frac{\mathrm{d}^2u_n}{\mathrm{d}t^2} = k(u^R_{n-1} + u^L_n - 2u_n) + C_s\frac{\mathrm{d}}{\mathrm{d}t}(u^R_{n-1} + u^L_n - 2u_n). \tag{A8a}$$

- the linkage part m (for x directional longitudinal motion and spinning)

$$(T_n^L - T_n^R)\cos\alpha_{\rm FC} = m\frac{{\rm d}^2}{{\rm d}t^2}\left(\frac{u_n^L + u_n^R}{2}\right), \tag{A8b}$$

$$-\frac{1}{2}L(T_n^L + T_n^R)\sin\beta = I_m\frac{{\rm d}^2\theta_n}{{\rm d}t^2}. \tag{A8c}$$

In the springs, the following relations must hold

$$T_n^L\cos\alpha_{\rm FC} = k(u_n - u_n^L) + {\rm C}_s\frac{\rm d}{{\rm d}t}(u_n - u_n^L), \tag{A8d}$$

$$T_n^R\cos\alpha_{\rm FC} = k(u_n^R - u_{n+1}) + {\rm C}_s\frac{\rm d}{{\rm d}t}(u_n^R - u_{n+1}). \tag{A8e}$$

By comparing equations (A8*a*)–(A8*e*) with equations (8*a*), (8*b*), (8*c*) and equations (9*a*), (9*b*), one can see that they are identical if one replaces the parameters α^0, L and F with $\alpha_{\rm FC}$, $L\sin\beta$ and $F_{\rm FC}$, respectively. Thus, the dispersion relation and the effective material parameters for the initially-folded spin-harnessed metamaterial can be easily obtained by using equations (16) and (17) with replacing the parameters properly:

$$-\left(M - \frac{p_{\rm FC}}{\omega^2}\right)\omega^2 = -\frac{A_{\rm FC}\cos\alpha_{\rm FC}}{\det\tilde{W}_{\rm FC}}(\exp(-{\rm i}qD) + \exp({\rm i}qD) - 2)$$
$$= -4\frac{A_{\rm FC}\cos\alpha_{\rm FC}}{\det\tilde{W}_{\rm FC}}\sin^2\frac{qD}{2}, \tag{A9a}$$

$$p_{\rm FC} = 2\tilde{k} - \frac{1}{\det\tilde{W}_{\rm FC}}(2\tilde{k} - 2A_{\rm FC}\cos\alpha_{\rm FC} - 2B_{\rm FC}\cos\alpha_{\rm FC}), \tag{A9b}$$

$$\tilde{W}_{\rm FC} = \begin{bmatrix} 1 - B_{\rm FC}\cos\alpha_{\rm FC}/\tilde{k} & A\cos\alpha_{\rm FC}/\tilde{k} \\ A_{\rm FC}\cos\alpha_{\rm FC}/\tilde{k} & 1 - B\cos\alpha_{\rm FC}/\tilde{k} \end{bmatrix}, \tag{A9c}$$

$$A_{\rm FC} = \frac{\omega^2 I_m F_{\rm FC}}{L\sin\beta} - \frac{\omega^2 m}{4\cos\alpha_{\rm FC}}, \tag{A9d}$$

$$B_{\rm FC} = \frac{\omega^2 I_m F_{\rm FC}}{L\sin\beta} + \frac{\omega^2 m}{4\cos\alpha_{\rm FC}}, \tag{A9e}$$

$$F_{\rm FC} = (2a_{\rm FC} - L\cos\theta_{\rm FC}^0)/a_{\rm FC}L\cos\theta_{\rm FC}^0, \tag{A9f}$$

$$\tilde{k} = k + {\rm i}\omega C_s, \tag{A9g}$$

$$M_{\rm eff} = M - \frac{p_{\rm FC}}{\omega^2}, \tag{A9h}$$

$$K_{\rm eff} = -\frac{A_{\rm FC}\cos\alpha_{\rm FC}}{\det\tilde{W}_{\rm FC}}. \tag{A9i}$$

In calculating the dispersion relation for the folded case, we note that $a_{\rm FC}$ and $\alpha_{\rm FC}$ are related to each other as

$$a_{\rm FC}^2 + b^2 - 2a_{\rm FC}b\cos\alpha_{\rm FC} = (L/2)^2. \tag{A10a}$$

Also, the angle β defined at the initially folded state can be calculated from $a_{\rm FC}$ and $\alpha_{\rm FC}$ as:

$$\frac{L}{2\sin\alpha_{\rm FC}} = \frac{a_{\rm FC}}{\sin\beta}. \tag{A10b}$$

Figure A2 plots the dispersion curves, effective mass and spring coefficients for various initial folded structures with $\alpha_{\rm FC}$ values. (For this figure, the lossless condition was used to clearly demonstrate the effects of $\alpha_{\rm FC}$.) Here, the same parameters shown in equation (35) were used except the α^0 and a values. Interestingly, one can see that the upper edge frequency of the first Bragg gap, 21.22 Hz, is little affected by the initial folding parameters $\alpha_{\rm FC}$, while the lower edge frequency of the second Bragg gap is highly affected by them. In fact, the upper edge frequency of the first Bragg gap, which is the main topic in this research, is not a function of the initial folding parameters.

To discuss the phenomenon occurring at the upper edge frequency of the first Bragg gap, it is noted that the upper edge frequency of the first Bragg gap and the lower edge frequency of the second Bragg gap correspond to infinite or negative-infinite effective stiffness $K_{\rm eff}$. To explain this, we note that $K_{\rm eff} = -A_{\rm FC}\cos\alpha_{\rm FC}/\det\tilde{W}_{\rm FC}$ becomes infinite or negative-infinite when $\det\tilde{W}_{\rm FC} = 0$, implying that

$$\det\tilde{W}_{\rm FC} = \left(1 - \frac{B_{\rm FC}\cos\alpha_{\rm FC}}{k}\right)^2 - \left(\frac{A_{\rm FC}\cos\alpha_{\rm FC}}{k}\right)^2 = 0. \tag{A11}$$

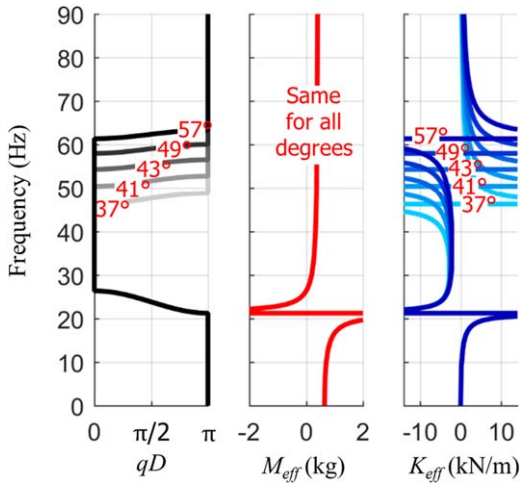

Figure A2. The dispersion curve, effective mass and spring coefficients for various α_{FC} of 37°, 41°, 43°, 49° and 57°. Note that in our numerical and experimental investigation, $\alpha^0 = 45°$ is used.

After some calculation, one can show the solution (ω) to equation (A11) satisfies the following equation:

$$\left(1 - \frac{\omega^2 m}{2k}\right)\left(1 - \frac{2\omega^2 I_m F_{FC} \cos \alpha_{FC}}{kL \sin \beta}\right) = 0. \tag{A12}$$

Solving equation (A12), one can derive

$$\text{The upper edge freq. of the 1st Bragg gap: } \omega^2 = 2k/m, \tag{A13a}$$

$$\text{The lower edge freq. of the 2nd Bragg gap: } \omega^2 = kL \sin \beta / I_m F_{FC} \cos \alpha_{FC}. \tag{A13b}$$

Equations (A13*a*) and (A13*b*) show that the upper edge frequency of the first Bragg gap is a function of the spring and mass coefficient only, while the lower edge frequency of the second Bragg gap is a function of several parameters including F_{FC} and α_{FC} that vary with the initial folding parameters (a_{FC} and α_{FC}). As our main interest in this research is on the first Bragg gap formed at zero or extremely low frequencies, the analysis in this section shows that the Bragg gap formed by the spin-harnessed metamaterial is very robust and not significantly affected by the initial folding condition. This can be an advantage if one considers to apply the spin-harness metamaterial approach in various low-frequency vibration shielding applications.

A2. Stabilizing the spin-harnessed metamaterial

Although the spin-harnessed metamaterial can provide a broad Bragg gap in an extremely low frequency range, it cannot sustain any static force since the spin-harnessed metamaterial has a zero stiffness at the static limit. Therefore, some special treatment is needed when the spin-harnessed metamaterial system is used in actual applications for vibration or noise shielding. There can be various ways to stabilize the spin-harnessed metamaterial, such as connecting the heavier mass M and the lighter mass m by an additional spring. Here, we will consider a method based on elastic foundation [26, 27] for stabilization. Figure A3(a) shows the spinning mass–spring system with an elastic foundation spring of stiffness G. The spring G is newly introduced between the heavier mass M and an external fixed boundary. Obviously, the use of G stabilizes the system, i.e., a static force applied to the system is responded by the spring G. The question is how much it affects the formed Bragg gap.

For the analysis, we note that the spring G affects the effective mass coefficient at extremely low frequencies around the static limit [26, 27]. In this case, the effective mass of the elastically-supported spinning mass–spring can be written as

$$M_{\text{eff}}^{G} = M_{\text{eff}} - \frac{G}{\omega^2}, \tag{A14}$$

where M_{eff} is the effective mass coefficient of the spin-harnessed metamaterial defined in equation (17). As can be seen in equation (A14), the additional term of $-G/\omega^2$ is introduced due to the spring G.

Figure A3(c) plots the dispersion curve, effective mass and spring coefficients of the elastically-supported spinning mass–spring system. The spring G contributes to make the effective mass coefficient negative at a very low frequency range, as reported in the previous researches [26, 27]. Accordingly, a new stop band is formed from 0 Hz to f_3 Hz; this stop band originates from the single negative material parameter (more specifically,

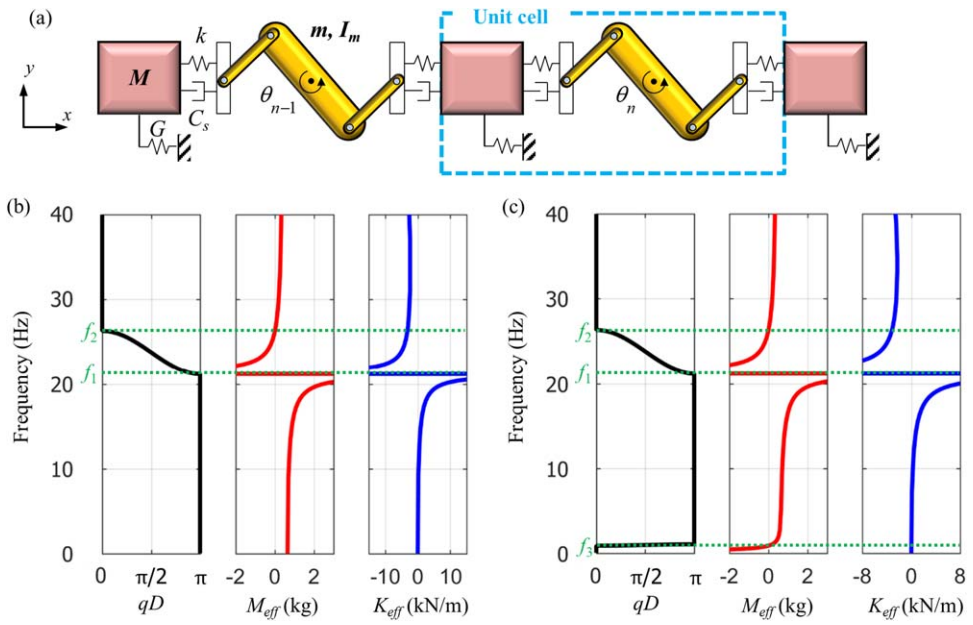

Figure A3. (a) The spin-harnessed metamaterial elastically supported by the foundation spring G. The dispersion curves, effective mass and spring coefficients for (b) $G = 0$ N m^{-1} and (c) $G = 20$ N m^{-1}.

negative mass and positive stiffness) so that it is not a Bragg gap. However, the comparison of the dispersion curves in figures A3(b) and (c) shows that the upper edge frequency of the Bragg gap, f_1, is almost unaltered by the presence of the spring G. Furthermore, the pass band generated around f_3 is almost flat. Because wave propagation in a flat branch is highly affected by damping, the whole frequency range below f_1 can practically work as a stop band. Here, we emphasize that only a narrow stop band from 0 Hz to f_3 Hz would be formed if the spin-harnessed metamaterial were not used. The analysis in section shows that a broad, extremely low-frequency stop band can be formed stably if the spin-harnessed metamaterial with elastic foundation is used.

References

[1] Sigalas M and Economou E N 1993 Band structure of elastic waves in two dimensional systems *Solid State Commun.* **86** 141
[2] Kushwaha M S, Halevi P, Dobrzynski L and Djafari-Rouhani B 1993 Acoustic band structure of periodic elastic composites *Phys. Rev. Lett.* **71** 2022
[3] Khelif A, Choujaa A, Benchabane S, Djafari-Rouhani B and Laude V 2004 Guiding and bending of acoustic waves in highly confined phononic crystal waveguides *Appl. Phys. Lett.* **84** 4400
[4] Khelif A, Djafari-Rouhani B, Vasseur J and Deymier P 2003 Transmission and dispersion relations of perfect and defect-containing waveguide structures in phononic band gap materials *Phys. Rev.* B **68** 024302
[5] Oudich M, Assouar B and Hou Z 2010 Propagation of acoustic waves and waveguiding in a two-dimensional locally resonant phononic crystal plate *Appl. Phys. Lett.* **97** 193503
[6] Oh J H, Lee I K, Ma P S and Kim Y Y 2011 Active wave-guiding of piezoelectric phononic crystals *Appl. Phys. Lett.* **99** 083505
[7] Lee I K, Kim Y J, Oh J H and Kim Y Y 2013 One-dimensional broadband phononic crystal filter with unit cells made of two non-uniform impedance-mirrored elements *AIP Adv.* **3** 022105
[8] Wang J, Xu X, Liu X and Xu G 2009 A tunable acoustic filter made by periodical structured materials *Appl. Phys. Lett.* **94** 181908
[9] Wu L-Y, Wu M-L and Chen L-W 2009 The narrow pass band filter of tunable 1D phononic crystals with a dielectric elastomer layer *Smart Mater. Struct.* **18** 015011
[10] Akjouj A, Al-Wahsa H, Sylla B, Djarafi-Rouhani B and Dobrzynsky L 2004 Stopping and filtering waves in phononic circuits *J. Phys.: Condens. Matter* **16** 37
[11] Liang B, Guo X S, Tu J, Zhang D and Cheng J C 2010 An acoustic rectifier *Nat. Mater.* **9** 989
[12] Li X–F, Ni X, Feng L, Lu M–H, He C and Chen Y–F 2011 Tunable unidirectional sound propagation through a sonic-crystal-based acoustic diode *Phys. Rev. Lett.* **106** 084301
[13] Zhu X, Zou X, Liang B and Cheng J 2010 One-way mode transmission in one-dimensional phononic crystal plates *J. Appl. Phys.* **108** 124909
[14] Oh J H, Kim H W, Ma P S, Seung H M and Kim Y Y 2012 Inverted bi-prism phononic crystals for one-sided elastic wave transmission applications *Appl. Phys. Lett.* **100** 213503
[15] Liu Z, Zhang X, Mao Y, Zhu Y Y, Yang Z, Chan C T and Sheng P 2000 Locally resonant sonic materials *Science* **8** 1734
[16] Huang H H, Sun C T and Huang G L 2009 On the negative effective mass density in acoustic metamaterials *Int. J. Eng. Sci.* **47** 610
[17] Zhu R, Liu X N, Hu G K, Sun C T and Huang G L 2014 A chiral elastic metamaterial beam for broadband vibration suppression *J. Sound Vib.* **333** 2759
[18] Zhu R, Liu X N, Hu G K, Sun C T and Huang G L 2014 Negative refraction of elastic waves at the deep-subwavelength scale in a single-phase metamaterial *Nat. Commun.* **5** 5510

[19] Romero-Garcia V, Krynkin A, Garcia-Raffi L M, Umnova O and Sanchez-Perez J V 2013 Multi-resonant scatterers in sonic crystals: locally multi-resonant acoustic metamaterial *J. Sound Vib.* **332** 184
[20] Oudich M, Senesi M, Assouar B M, Ruzenne M, Sun J–H, Vincent B, Hou Z and Wu T–T 2011 Experimental evidence of locally resonant sonic band gap in two-dimensional phononic stubbed plates *Phys. Rev.* B **84** 165136
[21] Williams E G, Roux P, Rupin M and Kuperman W A 2015 Theory of multiresonant metamaterials for A_0 Lamb waves *Phys. Rev.* B **91** 104307
[22] Oh J H, Kwon Y E, Lee H J and Kim Y Y 2016 Elastic metamaterials for independent realization of negativity in density and stiffness *Sci. Rep.* **6** 23630
[23] Oh J H, Seung H M and Kim Y Y 2016 Adjoining of negative stiffness and negative density bands in an elastic metamaterial *Appl. Phys. Lett.* **108** 093501
[24] Lee S H, Park C M, Seo Y M, Wang Z G and Kim C K 2009 Acoustic metamaterial with negative density *Phys. Lett.* A **373** 4464
[25] Lee S H, Park C M, Seo Y M, Wang Z G and Kim C K 2009 Acoustic metamaterial with negative modulus *J. Phys.: Condens. Matter* **21** 175704
[26] Yao S, Zhou X and Hu G 2010 Investigation of the negative-mass behaviors occurring below a cut-off frequency *New J. Phys.* **12** 103025
[27] Yu D, Wen J, Shen H, Xiao Y and Wen X 2012 Propagation of flexural wave in periodic beam on elastic foundations *Phys. Lett.* A **376** 626
[28] Oh J H and Assouar B 2016 Quasi-static stop band with flexural metamaterial having zero rotational stiffness *Sci. Rep.* **6** 33410
[29] Brillouin L 1946 *Wave Propagation in Periodic Structures* (New York: Dover)
[30] Liu X N, Hu G K, Huang G L and Sun C T 2011 An elastic metamaterial with simultaneously negative mass density and bulk modulus *Appl. Phys. Lett.* **98** 251907
[31] Bigoni D, Guenneau S, Movchan A B and Brun M 2013 Elastic metamaterials with inertial locally resonant structures: application to lensing and localization *Phys. Rev.* B **87** 174303
[32] Yilmaz C, Hulbert G M and Kikuchi N 2007 Phononic band gaps induced by inertial amplification in periodic media *Phys. Rev.* B **76** 054309
[33] Frandsen N M M, Bilal O R, Jensen J S and Hussein M I 2016 Inertial amplification of continuous structures: large band gaps from small masses *J. Appl. Phys.* **119** 124902
[34] Taniker S and Yilmaz C 2017 Generating ultra wide vibration stop bands by a novel inertial amplification mechanism topology with flexure hinges *Int. J. Solid Struct.* **106–107** 129
[35] Zheng L-Y, Tournat V and Gusev V 2017 Zero-frequency and extremely slow elastic edge waves in mechanical granular graphene *Ext. Mech. Lett.* **12** 55
[36] Zheng L-Y, Pichard H, Tournat V, Theocharis G and Gusev V 2016 Zero-frequency and slow elastic modes in phononic monolayer granular membranes *Ultrasonics* **69** 201
[37] Allein F, Tournat V, Gusev V E and Theocharis G 2017 Transversal-rotational and zero group velocity modes in tunable magneto-granular phononic crystals *Ext. Mech. Lett.* **12** 65
[38] Liang Z and Li J 2012 Extreme acoustic metamaterial by coiling up space *Phys. Rev. Lett.* **108** 114301
[39] Xie Y, Popa B-I, Zigoneanu L and Cummer S A 2013 Measurement of a broadband negative index with space-coiling acoustic metamaterials *Phys. Rev. Lett.* **110** 175501
[40] Liang Z *et al* 2013 Space-coiling metamaterials with double negativity and conical dispersion *Sci. Rep.* **3** 1614